

## Real-space Raman spectroscopy of graphene isotope superlattices

Whiteway, Eric; Lee, Martin; Hilke, Michael

**DOI**

[10.1103/PhysRevB.102.235429](https://doi.org/10.1103/PhysRevB.102.235429)

**Publication date**

2020

**Document Version**

Final published version

**Published in**

Physical Review B

**Citation (APA)**

Whiteway, E., Lee, M., & Hilke, M. (2020). Real-space Raman spectroscopy of graphene isotope superlattices. *Physical Review B*, 102(23), Article 235429. <https://doi.org/10.1103/PhysRevB.102.235429>

**Important note**


To cite this publication, please use the final published version (if applicable). Please check the document version above.

**Copyright**

Other than for strictly personal use, it is not permitted to download, forward or distribute the text or part of it, without the consent of the author(s) and/or copyright holder(s), unless the work is under an open content license such as Creative Commons.

**Takedown policy**

Please contact us and provide details if you believe this document breaches copyrights. We will remove access to the work immediately and investigate your claim.

**Real-space Raman spectroscopy of graphene isotope superlattices**Eric Whiteway,<sup>1</sup> Martin Lee<sup>1,2</sup> and Michael Hilke<sup>1,3</sup><sup>1</sup>*Department of Physics, McGill University, Montréal, Quebec, Canada H3A 2T8*<sup>2</sup>*Kavli Institute of Nanoscience, Delft University of Technology, Lorentzweg 1, 2628 CJ, Delft, Netherlands*<sup>3</sup>*Center for the Physics of Materials, Department of Physics, McGill University, Regroupement Québécois sur les Matériaux de Pointe, Montréal, Quebec, Canada H3A 2T8* (Received 23 July 2020; revised 30 November 2020; accepted 3 December 2020; published 23 December 2020)

We report the Raman spectroscopy of  $^{12}\text{C}/^{13}\text{C}$  graphene isotope superlattices (SLs) synthesized by chemical vapor deposition. At large periods the Raman spectrum corresponds to the sum of the bulk  $^{12}\text{C}$  and  $^{13}\text{C}$  contributions. However, at small periods we observe the formation of mixed  $^{12}\text{C}/^{13}\text{C}$  modes for Raman processes that involve two phonons, which results in the tripling of the  $2D$  and  $2D'$  Raman peaks. This tripling can be well understood in the framework of real-space Raman spectroscopy, where the two emitted phonons stem from different regions of the SL. The intensity of the mixed peak increases as the SL half-period approaches the mean free path of the photoexcited electron-hole pairs. By varying the SL period between 6 and 225 nm we have a direct measure of the photoexcited electron mean free path, which is found to be 18 nm for suspended graphene and 7 nm for graphene on  $\text{SiO}_2$  substrates.

DOI: [10.1103/PhysRevB.102.235429](https://doi.org/10.1103/PhysRevB.102.235429)**I. INTRODUCTION**

Raman spectroscopy is a powerful technique to measure vibrational energies through inelastic photoexcited electron scattering processes via the emission or absorption of phonons. These processes are typically viewed in momentum space, where momentum conservation plays an important role in the electron-phonon scattering processes. However, in the presence of short-range spatial variations of the phonon modes, real-space considerations become important. This is particularly relevant when the electronic degrees of freedom are spatially invariant as opposed to the vibrational properties. For instance, this is true in crystals, where the isotopes of the atoms have a spatial dependence, since the different masses will modify the vibrational properties, but not the electronic ones. Particularly interesting is the case in a single Raman process, where it is possible to generate two phonons from two regions with different atomic masses. This would lead to additional second-order Raman lines, which we discuss below.

The Raman spectrum of graphene is quite unique due to the prominence of two-phonon Raman processes. Indeed, the strongest Raman peak in pure graphene is the two-phonon  $2D$  Raman peak [1–3]. Isotope superlattices (SLs) composed of alternating bands of  $^{12}\text{C}$  and  $^{13}\text{C}$  result in a spatial variation of the phonon local density of states while preserving the crystal structure and electronic properties of graphene. They are therefore an ideal platform to investigate real-space Raman processes. In this work we report the synthesis of isotopic graphene SLs with periods as low as 6 nm and the resulting structure-dependent tripling of the two-phonon Raman peaks. We show that this peak structure is caused by a nonlocal Raman processes involving the emission of two spatially separated phonons and provides a direct measure of the mean free path of photoexcited electrons. Thus, Raman scattering

provides a unique tool to probe the spatial variation of phonon modes at scales much smaller than the optical wavelength.

Graphene isotopic SLs have been extensively studied theoretically using molecular dynamics [4–9] with a focus on thermal conductivity and acoustic phonons as opposed to the effect of the SL structure on the optical phonon modes. However, there have not been experiments on isotopic SLs until very recently [10], where a strong suppression of the thermal conductivity was observed due to the isotope heterointerface.

Three-dimensional SLs made from alternating layers of different materials or isotopes have been shown to demonstrate many novel properties, such as reduced thermal conductivity [11,12], increased mechanical strength [13,14], and modifications to the electronic [15] and phonon band structures [16,17]. Changes to the isotope content of fullerenes [18], nanotubes [19], diamond [20], and graphene [21] as well as other materials such as Ge [22] have been shown to modify phonon energies.

In this work, graphene SLs are synthesized by chemical vapor deposition (CVD) with a sequence of alternating  $^{12}\text{C}$  and  $^{13}\text{C}$  methane gas flow as diagramed in Fig. 1. Contrary to three-dimensional semiconductor SLs synthesized by molecular beam epitaxy, where the material is grown vertically, CVD of graphene proceeds by surface diffusion and aggregation. The result is a single layer of graphene with in-plane mass periodicity. Samples are composed of graphene single crystals with a radial sequence of alternating bands of  $^{12}\text{C}$  and  $^{13}\text{C}$ . These are characterized by a spatial period  $L_s$  varying between 6 and 225 nm. The synthesis is described in detail in Sec. VI. Characterization of these samples is done by a detailed study of the spatial dependence of the Raman peak intensities and energies as described in Secs. III and VII.

Interest in SLs is primarily motivated by the expected reduction in thermal conductivity [14,23,24] and the unique

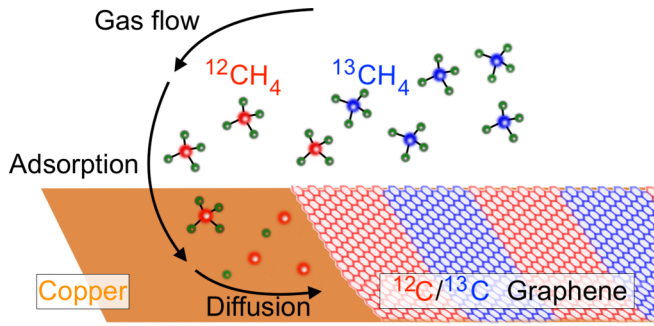


FIG. 1. Schematic of CVD growth of a graphene isotope SL.

properties of graphene [25–27], which may make a graphene SL an ideal material for thermoelectric devices. The synthesis of nanometer-scale graphene SLs with tunable interface density therefore represents an important advancement and we present a framework to directly characterize the isotope concentration and SL period in graphene and other two-dimensional materials through Raman spectroscopy.

To understand the effects of spatial variations in the phonon modes on Raman spectroscopy, it is important to consider the real-space Raman picture (see Figs. 2 and 3), which we describe next.

## II. REAL-SPACE RESONANT RAMAN PROCESSES

In general, Raman spectroscopy of graphene will identify a number of phonon energies at well-defined regions in momentum space. For instance, the so-called  $G$  peak corresponds to an emission (Stokes) or absorption (anti-Stokes) of phonons at the  $\Gamma$  point in the Brillouin zone. The most prominent peak ( $2D$ ) corresponds to two phonons close to the  $K$  (or  $K'$ ) points along the in-plane transverse optical phonon mode with wave number determined by the laser energy [28].

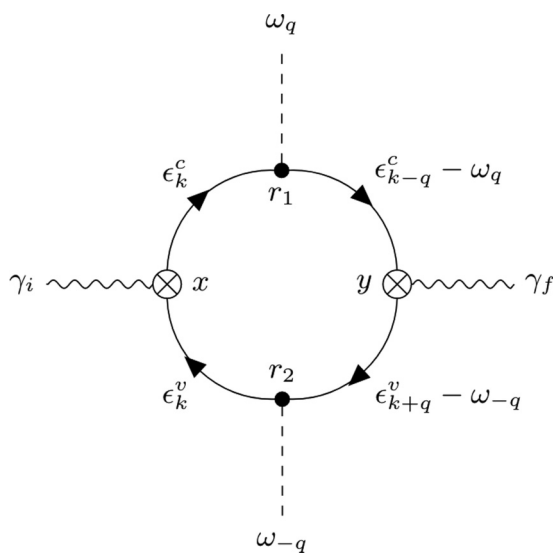


FIG. 2. An example of a two-phonon Stokes Feynman diagram for the  $2D$  or  $2D'$  resonant Raman scattering process. Here  $\gamma_{i,f}$  are the incoming and Raman-shifted outgoing photon energies,  $\omega_{\pm q}$  are the emitted phonon energies, and  $\epsilon_k^{c,v}$  are the electron and hole energies.

In graphene, the strong  $2D$  and narrow  $2D'$  peaks in Stokes Raman spectroscopy arise from the emission of two nonzero momentum phonons. Their higher amplitude than their single-phonon counterpart ( $D$  and  $D'$ ) can be explained by their double or triple resonant structure [1,29] or the sliding mechanism [30] due to the linear electronic dispersion.

This process and all the other relevant diagrams can be evaluated with standard diagrammatic techniques and summed up to obtain the full cross section. However, we will restrict the discussion to the process shown in Fig. 2, which involves intermediate states that are all real electronic states (not virtual), which will give a dominant contribution [31]. The diagram in Fig. 2, shown in the real (position) -space representation, is usually computed in momentum space [29], but here we will evaluate the diagram semiclassically in real space. This real-space approach is necessary, because our system lacks translational invariance, due to the periodic isotope structure. We therefore consider the real-space theory of resonant multiphonon Raman scattering proposed by Basko [31,32].

The real-space calculations of Raman processes were previously employed by Martin [33] for one-phonon Raman processes and Zeyher [34] for two-phonon Raman processes. This approach was extended by Basko and co-workers to calculate the intensities of Raman processes in graphene [31,35] and peak shapes in magneto-Raman processes [36]. Calculating the Raman matrix elements in the coordinate representation gives rise to a quasiclassical interpretation of the two-phonon Raman process, which we describe below.

The incoming light of energy  $\gamma_i$  produces an electron and a hole at  $x$  with opposite group velocity  $v = \partial_k \epsilon_k$ , where  $\epsilon_k$  is given by the hallmark conical dispersion relation of graphene,  $v \simeq 10^6$  m/s, and momentum  $k = \frac{\gamma_i}{2v}$ . The quasifree electron and hole will follow their initial trajectories of opposite velocity until they scatter with other electrons or phonons. If the electron scatters with a phonon of momentum  $q$  at  $r_1$  and the hole scatters with a phonon of momentum  $-q$  at  $r_2$ , they can eventually recombine at  $y$  and emit a Raman-shifted photon.

What is important in our context is that the two phonons involved are spatially separated due to the finite momentum transfer between electron holes and phonons. While many processes can contribute to the two-phonon Raman scattering amplitude, the most important one is shown in Fig. 2. The Feynman diagram is drawn in the real-space configuration, where a photoexcited electron is created at  $x$  after a photon absorption of energy  $\gamma_i$ . The electron of energy  $\epsilon_k^c \simeq \gamma_i/2$  is scattered by a phonon of energy  $\omega_q$  and momentum  $q$  at  $r_1$ , while the hole of energy  $\epsilon_k^v = \epsilon_k^c - \gamma_i$  is scattered by a phonon of energy  $\omega_{-q}$  and momentum  $-q$  at  $r_2$ . The electron and hole recombine at  $y$  to emit a photon of energy  $\gamma_f = \gamma_i - \omega_q - \omega_{-q}$ .

A necessary condition for recombination is that neither the electron nor hole undergoes another scattering event. However, this is generally quite likely, which leads to the well-known suppression of Raman events. For the events that contribute to the Raman amplitude, if the electron is scattered by a  $^{12}\text{C}$  phonon at  $r_1$  and the hole is scattered by a  $^{13}\text{C}$  phonon at  $r_2$  then the phonon emitted by the electron will

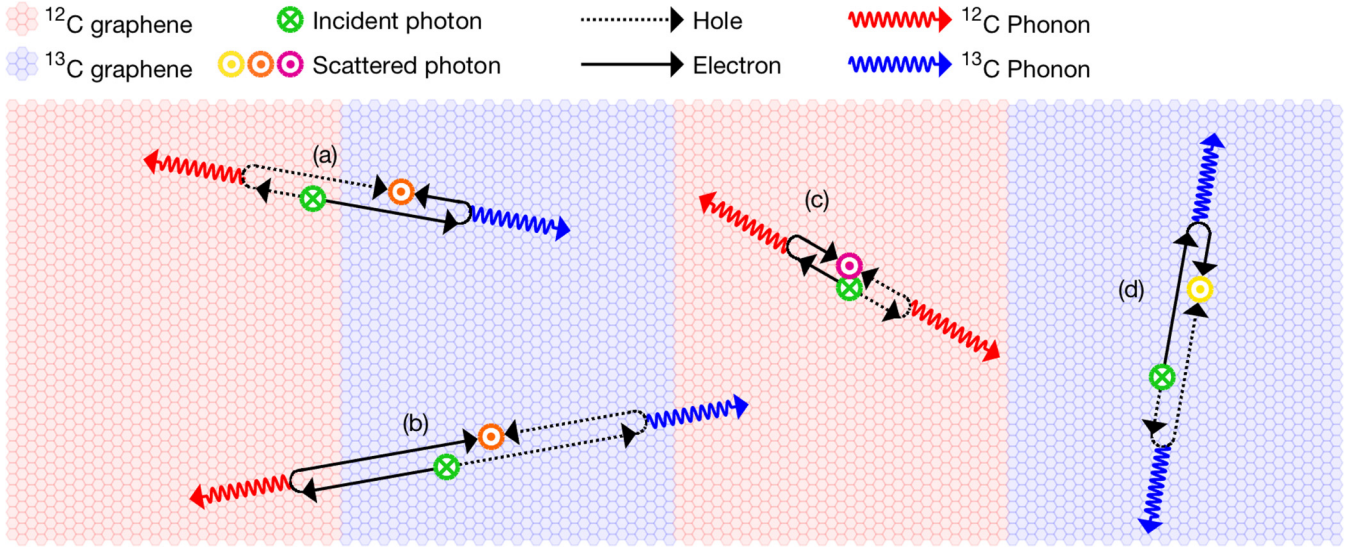


FIG. 3. Diagram of possible real-space Raman two-phonon processes in a  $^{12}\text{C}/^{13}\text{C}$  SL with energies given by (a)  $\omega^{13,12}$ , (b)  $\omega^{12,13}$ , (c)  $\omega^{12,12}$ , and (d)  $\omega^{13,13}$ . Solid and dotted lines represent the semiclassical trajectory of the photoexcited electron and hole, respectively. Note that, as described in Sec. II, the energy of the scattered photon is uniquely determined by the positions of phonon emission  $r_1$  and  $r_2$  and not the positions of the incident or emitted photon  $x$  and  $y$ .

have a different energy from the phonon emitted by the hole, yet both phonons will have opposite momenta. This process is illustrated in Fig. 3. This would lead to a combination Raman  $2D$  peak at an energy  $\omega_{2D} = \omega_D^{12} + \omega_D^{13}$ , where  $\omega_{2D}$  is the measured Raman  $2D$  peak shift and  $\omega_D^\alpha$  the  $D$ -phonon energy for isotope  $\alpha$ . In general, there will be three possible energies for the  $2D$  peak,  $\omega_{2D}^{\alpha\beta} = \omega_D^\alpha + \omega_D^\beta$ , where  $\alpha$  and  $\beta = 12$  or  $13$  as illustrated in Fig. 3 for an isotope SL. The typical separation between the electron and hole when they scatter with two phonons (not necessarily at the same time) is  $d_{e-h} = |r_1 - r_2| = \lambda$ , where  $\lambda$  is the electronic mean free path (MFP).

This real-space picture allows us to conveniently estimate the relative strengths of each process by identifying the corresponding spatial location probabilities of the electron and hole. If  $\tilde{r}_e(t)$  is the SL trajectory of the electron, then the probability to emit a phonon at  $r_1$  at time  $t_1$  and to recombine at  $y$  at time  $t = t_1 + t_2$  is proportional to  $e^{-t/\tau}$ , where  $\tau$  is the total scattering time. Equivalently, the probability for the hole with trajectory  $\tilde{r}_h(t)$  to emit a phonon at  $r_2$  at time  $t_2$  and to recombine at  $y$  at time  $t$  with the electron is also proportional

to  $e^{-t/\tau}$ , where we assume that the electron and hole have the same scattering time  $\tau$ . Therefore, the normalized joint probability for the electron to emit an  $\alpha$  phonon and for the hole to emit a  $\beta$  phonon is given by

$$P^{\alpha\beta}(\tilde{r}_e, \tilde{r}_h) = \left(\frac{2}{\tau}\right)^2 \int_0^\infty dt_1 \int_0^\infty dt_2 e^{-2(t_1+t_2)/\tau} \times M^\alpha[\tilde{r}_e(t_1)]M^\beta[\tilde{r}_h(t_2)], \quad (1)$$

where  $M^\alpha(r) = 1$  if we have isotope  $\alpha$  at position  $r$  and zero otherwise. We have  $M^{12}(r) + M^{13}(r) = 1$ . The relative integrated intensities of the two-phonon Raman peaks is then given by summing over all the electron and hole trajectory pairs

$$F^{\alpha\beta} = \frac{1}{N_{\text{tot}}} \sum_{\tilde{r}_e, \tilde{r}_h} P^{\alpha\beta}(\tilde{r}_e, \tilde{r}_h), \quad (2)$$

where  $F^{12,12} + F^{12,13} + F^{13,12} + F^{13,13} = 1$ . In the simple case of a one-dimensional isotope SL of period  $L_s$  in the direction  $x$  we have

$$F^{\alpha\beta} = \frac{2}{\pi \tau^2 L_s} \int_0^\infty dt_1 \int_0^\infty dt_2 \int_0^{L_s} dx \int_0^{2\pi} d\theta e^{-2(t_1+t_2)/\tau} M^\alpha[x + vt_1 \cos(\theta)] M^\beta[x - vt_2 \cos(\theta)]. \quad (3)$$

The relative fraction of integrated intensities  $F^{\alpha\beta}$  will depend on  $L_s$  and the electronic mean free path  $\lambda = v\tau$ . In the case of the  $2D$  and  $2D'$  modes the two permutations (12,13) and (13,12) are degenerate in energy and we write the relative intensity of the Raman signal as

$$F^{\{12,13\}} = F^{12,13} + F^{13,12}. \quad (4)$$

For  $\lambda \gg L_s$  all  $F^{\alpha\beta}$  are equal, while for  $\lambda \ll L_s$  we have  $F^{\{12,13\}} \simeq \frac{4\lambda}{\pi L_s}$  and a crossover region when  $\lambda \simeq L_s$ .

If we consider only the semiclassical trajectories of the electron-hole pair we find that the  $x$  component of the separation  $x_{e-h}$  is described by the distribution

$$P(x_{e-h}) = \frac{8}{\pi \lambda^2} x K_1\left(\frac{2x}{\lambda}\right), \quad (5)$$

where  $K_n$  is the Bessel function of the second kind. In the case of a SL with interface density  $I_d = 1/L_s$  this leads to a



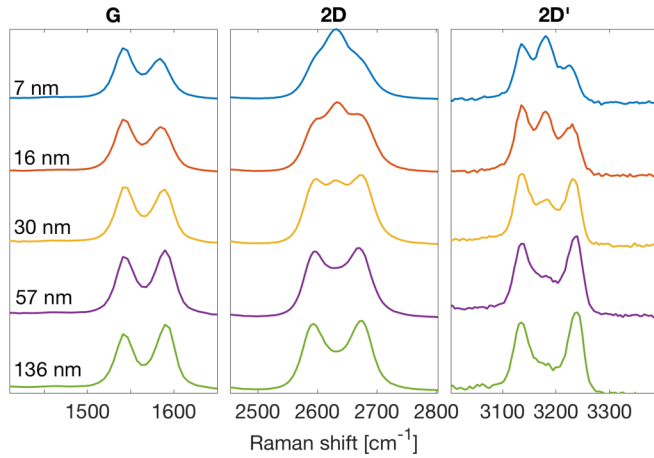


FIG. 4. Raman spectra as a function of SL period  $L_s$ . Spectra are averaged over 10–20 spots taken from a single sample with a wide range of periods.

dependence of  $F^{12,13}$  given by

$$F^{(12,13)} = \frac{1}{2} - \frac{4}{\pi^2} \sum_{n=1,3,5,\dots}^{\infty} \frac{1}{n^2(1+n^2\pi^2\lambda^2I_d^2)^{3/2}}. \quad (6)$$

The overall dependence can be well approximated numerically by

$$F^{(12,13)} \simeq \left[ \left( \frac{\pi L_s}{4\lambda} \right)^3 + f_0^{-3} \right]^{-1/3}, \quad (7)$$

where  $f_0$  is a constant determined by the duty cycle of  $^{12}\text{C}$  and  $^{13}\text{C}$  in the SL structure with  $f_0 = \frac{1}{2}$  in the case that the lengths of the  $^{12}\text{C}$  and  $^{13}\text{C}$  regions are equal. Equation (7) can be used to extract  $\lambda$  from  $L_s$  as discussed in the following sections.

### III. COMBINATION $^{12}\text{C}/^{13}\text{C}$ RAMAN PEAKS

$^{12}\text{C}/^{13}\text{C}$  graphene isotope SLs with periods ranging from 225 to 6 nm were prepared by CVD. The synthesis and characterization of these samples are described in Secs. VI and VII.

At SL periods greater than 100 nm we observe in Fig. 4, as expected, double peaks for each Raman mode in graphene corresponding to  $^{12}\text{C}$  and  $^{13}\text{C}$  graphene bulk Raman spectra. At small periods we also observe the formation of a third peak in the  $2D$  and  $2D'$  modes, as shown in Fig. 4. The additional middle Raman peaks arise from processes involving two spatially separated phonons, one  $^{12}\text{C}$  and one  $^{13}\text{C}$  phonon as described in detail in Sec. II. The frequencies and relative intensities of the peaks are extracted by fitting the  $2D$  and  $2D'$  modes with a triple Lorentzian peak structure. The Raman shift of this middle peak is the average of the  $^{12}\text{C}$  and  $^{13}\text{C}$  Raman peaks  $\omega_{2D}^{(12,13)} = \frac{1}{2}(\omega_{2D}^{12,12} + \omega_{2D}^{13,13})$  and the intensity  $F^{(12,13)}$  scales with decreasing SL period as given by Eq. (7). The experimental value of  $F^{(12,13)}$  is calculated as

$$F^{(12,13)} = \frac{N^{(12,13)}}{N^{12,12} + N^{13,13} + N^{(12,13)}}, \quad (8)$$

where  $N^{\alpha,\beta}$  are the integrated counts of the corresponding Raman peak, determined by fitting with a triple Lorentzian

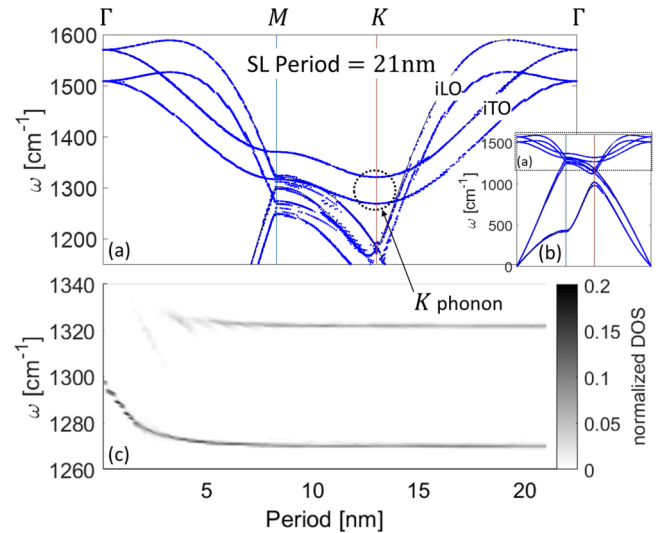


FIG. 5. Calculated SL phonon dispersion shown for a  $^{12}\text{C}/^{13}\text{C}$  SL of period 21 nm [blue dots in (a) and (b)]. (a) Close-up of the in-plane longitudinal and transverse optical (iLO and iTO, respectively) frequency range from the full dispersion in (b). The solid reference lines show the in-plane dispersion for pure  $^{12}\text{C}$ . (c) Graph showing the DOS for iTO phonons close to the  $K$  point ( $D$ -peak phonons) as a function of SL period [38].

(details of the spectral fitting are in the Supplemental Material [37]).

In the case of the one-phonon  $G$  process we do not observe the formation of a third peak. The observation that the third peak is only present for two-phonon Raman processes as well as the lack of any features in the calculated phonon density of states (DOS) for  $L_s > 6$  nm (see Fig. 5) corresponding to this intermediate peak strongly suggest that it results from a two-phonon process involving one  $^{12}\text{C}$  and one  $^{13}\text{C}$  phonon. It also precludes the possibility that this peak is simply the result of the underlying isotope distribution, since a distribution peaked at an isotope concentration  $\rho = 0.5$  would be evident in the  $G$  peak structure.

While the  $2D$  and  $2D'$  peaks involve two phonons on the same phonon branch (close to the  $K$  point for  $2D$  and close to  $\Gamma$  for  $2D'$ ), other combination peaks such as  $D' + D^3$  and  $D + D''$  involve two different phonon branches [39]. In this case  $\omega^{12,13} \neq \omega^{13,12}$ , which would lead to two additional phonon peaks as shown in the Supplemental Material [37].

For the  $2D$  and  $2D'$  Raman amplitudes, we find that the relative intensity  $F^{(12,13)}$  of the mixed Raman peak increases with decreasing SL period approximately as  $1/L_s$ . This is shown in Fig. 6. The dependence is well fitted by Eq. (7), which depends on the ratio of the SL period  $L_s$  and the MFP.

### IV. PHOTOEXCITED ELECTRON MEAN FREE PATH

The incoming Raman laser beam excites the electrons by the energy of the photon. With momentum conservation in the Dirac cone electron dispersion, most photoexcited electrons will have an energy close to  $\epsilon_L/2$  from the  $K$  point, where  $\epsilon_L$  is the incoming photon energy. These photoexcited electrons will rapidly decay to lower energies by inelastic scattering with other electrons and phonons. Time-resolved

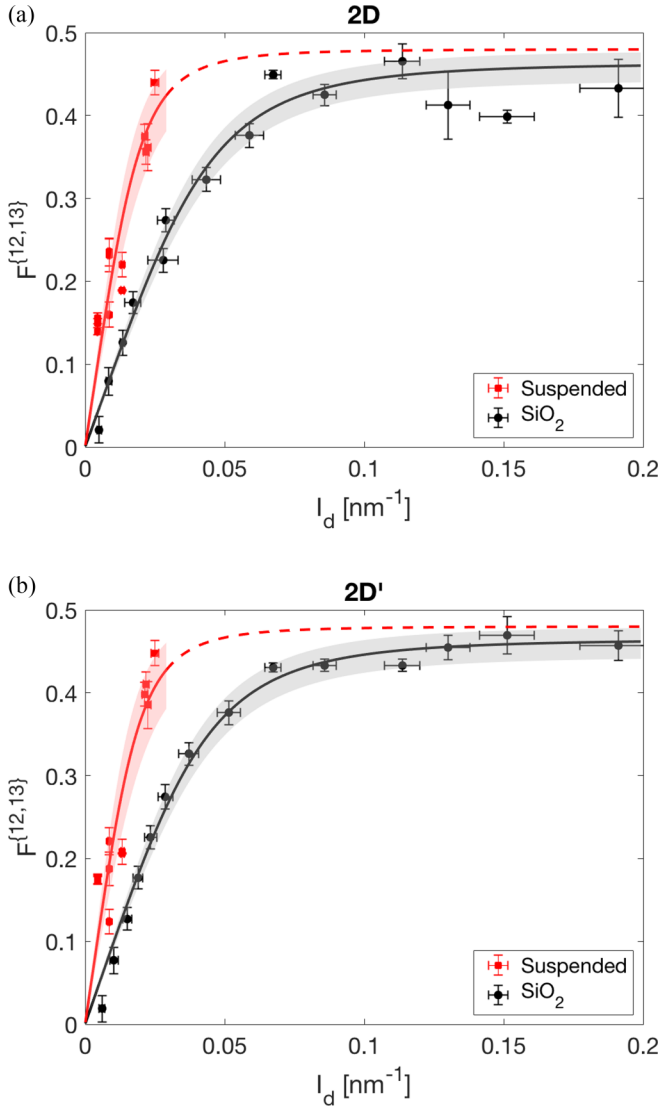


FIG. 6. Length dependence of the relative intensity of a mixed process Raman peak for the (a) 2D and (b) 2D' modes. Here  $F^{(12,13)}$  is plotted against the interface density  $I_d = 1/L_s$ . As expected, we observe at small values of  $I_d$  a linear dependence with slope determined by  $\lambda$ . Data points are determined by binning values corresponding to individual spectra and error bars show the standard error on the mean. The y error bars also include the experimental error on  $L_s$  determined by the spatial resolution of the Raman maps. The data are fit to Eq. (7) and the shaded error shows the 95% confidence interval of the fit parameters.

experiments in graphene show that this decay starts to happen in the 10 fs range [40]. Experiments and simulations seem to indicate that the initial electron-electron scattering is followed by electron-optical phonon scattering spanning 10–300 fs [40–42]. Time-resolved Raman spectroscopy experiments in graphite have shown the full building of the G phonon Raman mode to be below 300 fs with an initial buildup within 20 fs [43,44].

For the photoexcited electrons and holes, the total inelastic mean free time is given by  $\tau_{\text{tot}}^{-1} = \tau_{e\text{-ph}}^{-1} + \tau_{e\text{-e}}^{-1}$ , where  $\tau_{e\text{-e}}^{-1}$  is the electron-electron scattering rate and  $\tau_{e\text{-ph}}^{-1}$  is the electron-

TABLE I. Comparison of the present results with previous literature values of electronic linewidth in graphene, in order of increasing MFP. Here ARPES denotes angle-resolved photoemission spectroscopy and TRPES denotes time-resolved photoemission spectroscopy.

$2\gamma$ (meV)	$\lambda$ (nm)	Technique	Reference
100	6.6	ARPES	[47]
89	7.4	Raman SL (supported)	this work
66	10	Raman	[32]
54	12	magneto-Raman	[36]
48	14	Raman	[29]
36	18	Raman SL (suspended)	this work
<33	>20	ARPES (epitaxial)	[48]
28	24	TRPES (HOPG)	[49]

phonon scattering rate. For hot electrons and photoexcited electrons in graphene  $\tau_{\text{tot}}$  was calculated to be in the 10–120 fs range and dependent on the Fermi energy [45,46]. The time-resolved experiments discussed above are consistent with a shorter  $\tau_{e\text{-e}}$  compared to  $\tau_{e\text{-ph}}$ . In this case only a small fraction of the Raman photoexcited electrons will generate a Raman phonon.

The Raman analysis in the real-space picture gives us a direct measurement of the MFP of photoexcited electrons, which is connected to the total scattering time by  $\lambda = v\tau_{\text{tot}}$ . Using Eq. (7), we can fit the relative intensities as a function of superlattice period to obtain  $\lambda$ . This is shown in Fig. 6 for both suspended graphene and graphene supported on  $\text{SiO}_2$  and is in good agreement with the experimental data. A least-squares fit gives  $\lambda$  of  $18 \text{ nm} \pm 4 \text{ nm}$  in suspended graphene compared to  $7.4 \text{ nm} \pm 0.6 \text{ nm}$  in graphene on  $\text{SiO}_2$ .

While there are no other direct experimentally measured mean free paths of the photoexcited electrons or holes in graphene, various measurements have been made of the electronic linewidth and the exciton lifetime, by time- or angle-resolved photoemission spectroscopy or Raman experiments and report values ranging from 28 to 100 meV. Table I summarizes results measuring electronic broadening, excitation lifetime, and mean free path of carriers in graphene and highly oriented pyrolytic graphite (HOPG). The corresponding value of  $\lambda$  is obtained from  $\lambda = \hbar v / 2\gamma$ . Electronic broadening is reported depending on the reference as one of  $\gamma$ ,  $2\gamma$ , or  $4\gamma$  and here are standardized as  $2\gamma$ . Our measured values of  $\lambda$  correspond to values of  $2\gamma \simeq 36 \text{ meV}$  for suspended graphene and approximately 89 meV for graphene on  $\text{SiO}_2$ , which are similar to the other results reported in the literature.

The total probability of resonant two-phonon processes is proportional to  $\lambda^2$  [31]. Therefore, if we consider the Raman nonresonant G peak intensity to be independent of scattering rate then we expect the ratio  $I_{2D}/I_G \propto \lambda^2$ . The ratio  $I_{2D}/I_G$  has previously been shown to increase for suspended graphene vs graphene on  $\text{SiO}_2$  which was attributed to a decrease in charged impurities [50]. Similarly, we find that suspending graphene increases both the measured value of  $\lambda$  and  $I_{2D}/I_G$  compared to the results on  $\text{SiO}_2$  substrates. For suspended graphene the ratio  $I_{2D}/I_G \simeq 6$  whereas for supported graphene

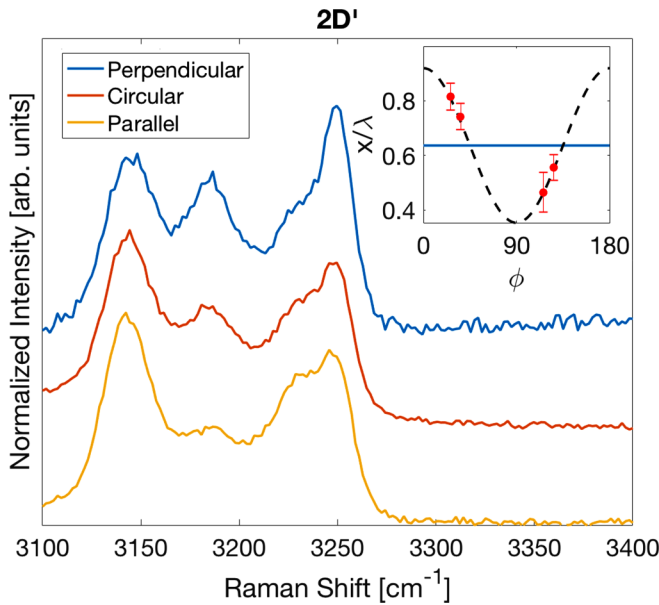


FIG. 7. Polarization dependence:  $2D'$  spectrum for circular and linear polarizations approximately perpendicular and parallel to the mass periodicity. The inset shows the theoretical polarization dependence of  $x/\lambda$  given by Eq. (9). Measured polarizations are shown in red with error bars calculated from the standard deviation of the spectral fitting parameters.

we measure  $I_{2D}/I_G \simeq 4$  (see Supplemental Material [37] for details).

## V. DEPENDENCE ON POLARIZATION

The real-space Raman process described in Sec. II will invariably lead to a dependence on the polarization of the incoming light with respect to the SL orientation, since the photoexcited electron-hole pair will more likely have a momentum perpendicular to the polarization. For an angle  $\phi$  measured between the electric field polarization and the electron-hole pair momenta the probability of detecting a photon [31], corresponding to the backscattered electron-hole pair, varies as  $(\sin \phi)^4$ . Hence, electron-hole pairs with momenta in the direction of periodicity will more likely result in the emission of 12–13 phonon pairs and as a result the value of  $F^{(12,13)}$  will vary as a function of polarization angle as shown in Fig. 7.

The magnitude of  $F^{(12,13)}$  is varied by the parameter  $x$ , the component of the mean free path in the direction of periodicity, which we take to be  $\frac{2}{\pi}\lambda$  for circularly polarized light. We can quantify the polarization dependence by considering the value of  $x(\phi)$  as a function of polarization angle  $\phi$  as

$$\frac{x(\phi)}{\lambda} = \frac{8}{3\pi} \int_0^\pi \sin(\theta) [\sin(\theta - \phi)]^4 d\theta. \quad (9)$$

The value of  $F^{(12,13)}$  is measured for different linear polarizations and the corresponding value of  $x$  is extracted by solving Eq. (7) for  $\lambda$ . We take  $\phi = 0$  to be polarized perpendicular to the periodicity of the SL. This is shown in the inset of Fig. 7. The number of experimental data points is limited, but is consistent with Eq. (9).

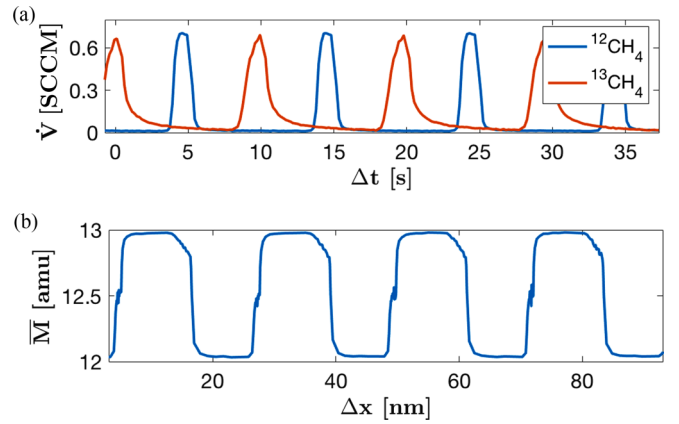


FIG. 8. (a) Growth log showing flow rates  $\dot{V}$  of  $^{12}\text{C}$  and  $^{13}\text{C}$  methane along with (b) the corresponding atomic mass vs distance, where distance is calculated as  $\dot{V}\Delta t$  and scaled to correspond to the measured growth rate and the average atomic mass is obtained from the isotopic methane concentration. Here SCCM denotes cubic centimeter per minute at STP.

## VI. SYNTHESIS OF ISOTOPE SUPERLATTICE

Graphene is grown by low-pressure chemical vapor deposition on commercially available 25- $\mu\text{m}$ -thick copper foils. During the growth phase  $^{12}\text{C}$  methane and  $^{13}\text{C}$  methane are pulsed in an alternating sequence. The methane sources are respectively 99.99% pure  $^{12}\text{C}$  methane or 99% pure  $^{13}\text{C}$  methane (Sigma-Aldrich 490229). The duration of the pulses is on the order of 1 s followed by a 2–4 s period with no methane flow in order to maintain high isotope concentration throughout the growth.

Periodically, a long (1-min) pulse of pure  $^{12}\text{C}$  or  $^{13}\text{C}$  methane is introduced which allows us to distinguish different regions and the associated isotope sequence in the graphene crystal and extract the SL period for each region. Regions consist of between 100 and 2000 gas pulses and result in average SL periods ranging from 6 to 225 nm. Figure 8 shows a typical gas flow sequence along with the associated isotope distribution as a function of radial distance. Growth conditions are chosen to produce isolated graphene single crystals and graphene is subsequently deposited onto Si/SiO<sub>2</sub> wafers by poly(methyl methacrylate) wet transfer for Raman spectroscopy.

## VII. CHARACTERIZATION OF THE GRAPHENE ISOTOPE SUPERLATTICE

In order to demonstrate the successful synthesis of an isotopic SL we perform a careful analysis of the measured gas flow rates during CVD growth and the Raman spectra of the resulting samples. Samples are characterized by Raman mapping using a Renishaw InVia system and a 514-nm laser excitation source.

Using the growth of a single crystal with regions of varying isotope concentration in 10% concentration steps [51], we can extract the Raman  $G$  peak position and width dependence on the  $^{12}\text{C}$  isotope concentration  $\rho$  for homogeneous isotope mixtures. We can fit the peak with a Lorentzian of width  $\gamma_\rho$

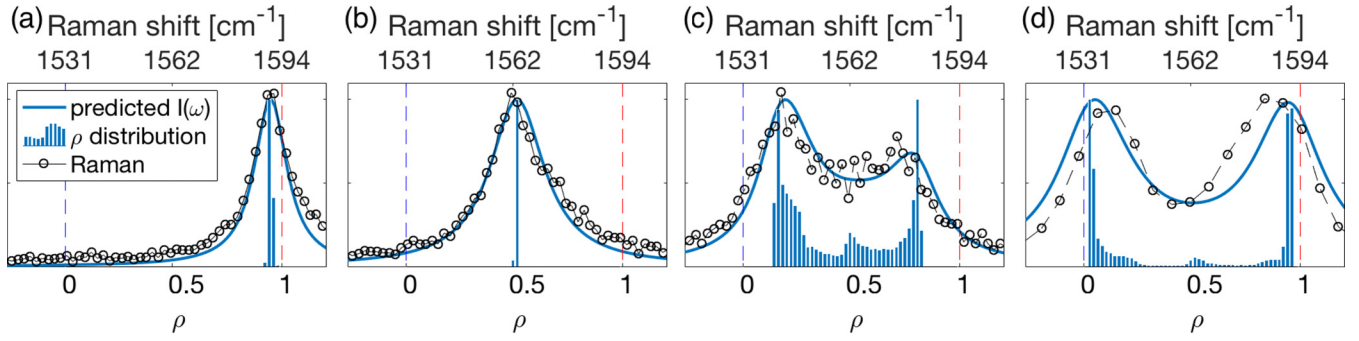


FIG. 9. Predicted vs measured  $G$  peak Raman spectra for different isotope distributions. The bar graph indicates the isotope concentration distribution extracted from the growth logs. The solid line is the predicted Raman peak shape from Eq. (12) and circles show the measured Raman spectra for the corresponding region. (a) 100%  $^{12}\text{C}$  graphene, (b) 50%  $^{12}\text{C}$  mix, (c) low-isotope-concentration superlattice ( $C \simeq 0.7$ ), and (d) high-isotope-concentration superlattice ( $C \simeq 0.9$ ). The measured Raman spectra represent a single map point, with short collection time, and as a result are relatively noisy. These are shown as is, in order to avoid introducing extra linewidth broadening by averaging over multiple data points.

and position  $\omega_\rho$ , where

$$\omega_\rho = \omega^{12} \sqrt{\frac{12}{13 - \rho}}, \quad \gamma_\rho = \gamma_0 + \gamma_1 \frac{f(\rho)}{f(0.5)}. \quad (10)$$

The  $f(\rho)$  was calculated by Rodriguez-Nieva *et al.* [21], who found for uncorrelated mass disorder

$$f(\rho) = \rho(1 - \rho)\delta m^2 (1 + \rho\delta m)^{-5/2}. \quad (11)$$

Here  $\delta m = \frac{1}{12}$  is the relative mass difference of  $^{13}\text{C}$  and  $^{12}\text{C}$ . We find  $\gamma_1 = 6.2 \text{ cm}^{-1}$  and  $\gamma_0 = 12.4 \text{ cm}^{-1}$ , in line with previously reported values [21,52] (details and figure shown in the Supplemental Material [37]).

It is now possible to predict the expected peak structure for an inhomogeneous distribution of isotopes, where the concentration of each dominant isotope region is not necessarily 100% pure as expected from the growth log shown in Fig. 8. We expect the inhomogeneous peak structure to be given by a sum of Lorentzian peaks weighted by the isotope concentration distribution  $P_\rho$ :

$$I(\omega) = \sum_\rho P_\rho \frac{\gamma_\rho/2}{(\omega - \omega_\rho)^2 + (\gamma_\rho/2)^2}. \quad (12)$$

As a result, we can now compare in Fig. 9 the measured Raman  $G$  peak structure with the expected peak structure from Eq. (12) using the measured isotope distribution from the gas flows of the growth (see Fig. 8). As we can see in Fig. 8, the peak concentrations are not exactly 100% or 0% in each isotope region and they depend on the growth as shown in Fig. 9, which justifies the use of Eq. (12). Examples of different binary distributions of concentrations are shown in Fig. 9 as well as the corresponding predicted Raman peak structure. The excellent agreement between the predicted and measured spectra indicates that the distribution of isotopes within the samples is well represented by the measured gas flows and that the Raman  $G$  peak is determined by the corresponding isotope distribution. As such we can use the  $G$  peak position and line shape as a measure of the SL purity.

For a bimodal isotope concentration distribution such as those shown in Figs. 9(c) and 9(d) we find that we can individually resolve the  $^{12}\text{C}$  and  $^{13}\text{C}$  Raman  $G$  peaks. We consider the

simplifying approximation that the concentration distribution is well described with two peaks centered at  $\rho_1$  and  $\rho_2$  and integrated peak counts  $N_1$  and  $N_2$  and therefore the Raman intensity is well described by considering two peaks with Raman shifts of  $\omega_1$  and  $\omega_2$  and integrated counts  $N_1$  and  $N_2$  where  $\omega_{1,2}$  and  $\rho_{1,2}$  are related through Eq. (10).

Two useful quantities describing the SL quality, the average carbon mass  $\bar{M}$  and the average isotopic concentration  $C$ ,

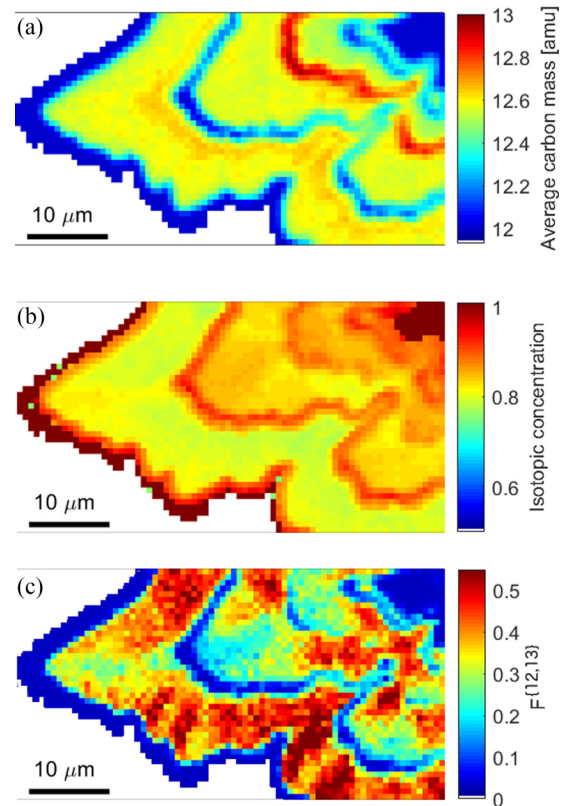


FIG. 10. Raman maps of (a) the average carbon mass  $\bar{M}$  using Eq. (13), (b) the isotopic concentration  $C$  using Eq. (14) and calculated from the  $G$  peak position and intensity, and (c) the measured mixed peak relative intensity  $F^{(12,13)}$ .



can be calculated from the  $G$  peak line shape as

$$\bar{M} = 13 - \frac{N_1\rho_1 + N_2\rho_2}{N_1 + N_2}, \quad (13)$$

$$C = \frac{\omega_2 - \omega_1}{2(\omega_G^{12} - \omega_G^{13})} + \frac{1}{2}, \quad (14)$$

where  $\omega_G^{12} - \omega_G^{13} \simeq 62 \text{ cm}^{-1}$ . In Fig. 10 these two quantities are shown for a given SL Raman map, extracted by fitting the  $G$  peak to a double Lorentzian function.

From the Raman maps shown in Fig. 10 we observe that the sample contains several regions with a periodic SL structure and average mass of approximately 12.5 amu separated by lines of pure  $^{12}\text{C}$  and  $^{13}\text{C}$  graphene. We note that the SL period is generally smaller than the spot size of the Raman excitation laser and as such each data point is averaging over several periods. We are able to realize isotopic concentrations from 0.8 to greater than 0.9. This assumes constant  $\omega_\rho$ , which is in agreement with our numeric results for SL periods greater than 10 nm.

In general, we also observe broadening of the Raman peaks compared to pristine  $^{12}\text{C}$  or  $^{13}\text{C}$  graphene, which we attribute to increased phonon scattering from isotope impurities [21] and a further broadening caused by the inhomogeneous isotope distribution within a given band. From the Raman map for each region (delimited by regions of pure  $^{12}\text{C}$  or  $^{13}\text{C}$

graphene) the average superlattice period  $L_s$  can be calculated by measuring the length of the region and the number of isotopic methane pulses employed in the growth phase.

## VIII. CONCLUSION

We presented experimentally realized Raman spectroscopy of nanometer-scale graphene isotope superlattices. Characterization of these superlattices shows evidence of high isotopic concentration greater than 0.9 and small superlattice period on the order of 6 nm. We found a mixed Raman process involving spatially separated phonons from both the  $^{12}\text{C}$  and  $^{13}\text{C}$  bands. The mixed Raman process is well explained quantitatively by the real-space Raman picture, involving two-phonon resonant Raman processes. The intensity of this process increases as a function of the superlattice interface density and depends on the mean free path of the photoexcited carriers involved in the Raman process. We show the dependence of the photoexcited electron mean free path on the substrate by comparing suspended and  $\text{SiO}_2$  supported graphene where the mean free paths was found to be 7.4 and 18 nm, respectively.

## ACKNOWLEDGMENTS

We acknowledge helpful discussions with Denis Basko. This work was supported by NSERC, FRQNT, and INTRIQ.

- 
- [1] C. Thomsen and S. Reich, *Phys. Rev. Lett.* **85**, 5214 (2000).
- [2] J. Maultzsch, S. Reich, C. Thomsen, H. Requardt, and P. Ordejón, *Phys. Rev. Lett.* **92**, 075501 (2004).
- [3] A. C. Ferrari, J. C. Meyer, V. Scardaci, C. Casiraghi, M. Lazzeri, F. Mauri, S. Piscanec, D. Jiang, K. S. Novoselov, S. Roth, and A. K. Geim, *Phys. Rev. Lett.* **97**, 187401 (2006).
- [4] T. Ouyang, Y. P. Chen, K. K. Yang, and J. X. Zhong, *Europhys. Lett.* **88**, 28002 (2009).
- [5] X. Mu, T. Zhang, D. B. Go, and T. Luo, *Carbon* **83**, 208 (2015).
- [6] I. M. Felix and L. F. C. Pereira, *Sci. Rep.* **8**, 2737 (2018).
- [7] Z. Xie, X. Chen, X. Yu, Y. Zhang, H. Wang, and L. Zhang, *Sci. China Phys. Mech. Astron.* **60**, 107821 (2017).
- [8] Y. Gu, *Numer. Heat Transfer A* **73**, 115 (2018).
- [9] M. Davies, B. Ganapathysubramanian, and G. Balasubramanian, *Appl. Phys. Lett.* **110**, 133107 (2017).
- [10] E. Whiteaway, M. Lee, and M. Hilke, *ACS Appl. Nano Mater.* **3**, 9167 (2020).
- [11] S. M. Lee, D. G. Cahill, and R. Venkatasubramanian, *Appl. Phys. Lett.* **70**, 2957 (1997).
- [12] R. Venkatasubramanian, *Phys. Rev. B* **61**, 3091 (2000).
- [13] S. Menezes and D. P. Anderson, *J. Electrochem. Soc.* **137**, 440 (1990).
- [14] P. Yashar, S. A. Barnett, J. Rechner, and W. D. Sproul, *J. Vac. Sci. Technol. A* **16**, 2913 (1998).
- [15] T. P. Pearsall, J. Bevk, L. C. Feldman, J. M. Bonar, J. P. Mannaerts, and A. Ourmazd, *Phys. Rev. Lett.* **58**, 729 (1987).
- [16] C. Colvard, R. Merlin, M. V. Klein, and A. C. Gossard, *Phys. Rev. Lett.* **45**, 298 (1980).
- [17] J. Spitzer, T. Ruf, M. Cardona, W. Dondl, R. Schorer, G. Abstreiter, and E. E. Haller, *Phys. Rev. Lett.* **72**, 1565 (1994).
- [18] S. Guha, J. Menéndez, J. B. Page, G. B. Adams, G. S. Spencer, J. P. Lehman, P. Giannozzi, and S. Baroni, *Phys. Rev. Lett.* **72**, 3359 (1994).
- [19] S. D. Costa, C. Fantini, A. Righi, A. Bachmatiuk, M. H. Rummeli, R. Saito, and M. A. Pimenta, *Carbon* **49**, 4719 (2011).
- [20] H. Watanabe and S. Shikata, *Diam. Relat. Mater.* **20**, 980 (2011).
- [21] J. F. Rodriguez-Nieva, R. Saito, S. D. Costa, and M. S. Dresselhaus, *Phys. Rev. B* **85**, 245406 (2012).
- [22] H. D. Fuchs, C. H. Grein, C. Thomsen, M. Cardona, W. L. Hansen, E. E. Haller, and K. Itoh, *Phys. Rev. B* **43**, 4835 (1991).
- [23] T. Yao, *Appl. Phys. Lett.* **51**, 1798 (1987).
- [24] M. V. Simkin and G. D. Mahan, *Phys. Rev. Lett.* **84**, 927 (2000).
- [25] K. S. Novoselov, A. K. Geim, S. V. Morozov, D. Jiang, Y. Zhang, S. V. Dubonos, I. V. Grigorieva, and A. A. Firsov, *Science* **306**, 666 (2004).
- [26] K. I. Bolotin, K. J. Sikes, Z. Jiang, M. Klima, G. Fudenberg, J. Hone, P. Kim, and H. L. Stormer, *Solid State Commun.* **146**, 351 (2008).
- [27] D. Dragoman and M. Dragoman, *Appl. Phys. Lett.* **91**, 203116 (2007).
- [28] L. M. Malard, M. A. Pimenta, G. Dresselhaus, and M. S. Dresselhaus, *Phys. Rep.* **473**, 51 (2009).
- [29] P. Venezuela, M. Lazzeri, and F. Mauri, *Phys. Rev. B* **84**, 035433 (2011).
- [30] E. J. Heller, Y. Yang, L. Kocia, W. Chen, S. Fang, M. Borunda, and E. Kaxiras, *ACS Nano* **10**, 2803 (2016).
- [31] D. M. Basko, *Phys. Rev. B* **78**, 125418 (2008).
- [32] D. M. Basko, S. Piscanec, and A. C. Ferrari, *Phys. Rev. B* **80**, 165413 (2009).

- [33] R. M. Martin, *Phys. Rev. B* **4**, 3676 (1971).
- [34] R. Zeyher, *Phys. Rev. B* **9**, 4439 (1974).
- [35] A. C. Ferrari and D. M. Basko, *Nat. Nanotechnol.* **8**, 235 (2013).
- [36] C. Faugeras, P. Kossacki, D. M. Basko, M. Amado, M. Sprinkle, C. Berger, W. A. de Heer, and M. Potemski, *Phys. Rev. B* **81**, 155436 (2010).
- [37] See Supplemental Material at <http://link.aps.org/supplemental/10.1103/PhysRevB.102.235429> for details of spectral fitting, polarization measurements, Raman peak characterization, combination Raman modes, and 2D peak intensity (as well as Refs. [21,31,50–52]).
- [38] E. Whiteway and M. Hilke (unpublished).
- [39] S. Bernard, E. Whiteway, V. Yu, D. G. Austing, and M. Hilke, *Phys. Rev. B* **86**, 085409 (2012).
- [40] M. Breusing, S. Kuehn, T. Winzer, E. Malić, F. Milde, N. Severin, J. P. Rabe, C. Ropers, A. Knorr, and T. Elsaesser, *Phys. Rev. B* **83**, 153410 (2011).
- [41] A. Tomadin, D. Brida, G. Cerullo, A. C. Ferrari, and M. Polini, *Phys. Rev. B* **88**, 035430 (2013).
- [42] D. Brida, A. Tomadin, C. Manzoni, Y. J. Kim, A. Lombardo, S. Milana, R. R. Nair, K. S. Novoselov, A. C. Ferrari, G. Cerullo, and M. Polini, *Nat. Commun.* **4**, 1987 (2013).
- [43] H. Yan, D. Song, K. F. Mak, I. Chatzakis, J. Maultzsch, and T. F. Heinz, *Phys. Rev. B* **80**, 121403(R) (2009).
- [44] K. Ishioka, M. Hase, M. Kitajima, L. Wirtz, A. Rubio, and H. Petek, *Phys. Rev. B* **77**, 121402(R) (2008).
- [45] W.-K. Tse, E. H. Hwang, and S. Das Sarma, *Appl. Phys. Lett.* **93**, 023128 (2008).
- [46] J. C. W. Song, K. J. Tielrooij, F. H. L. Koppens, and L. S. Levitov, *Phys. Rev. B* **87**, 155429 (2013).
- [47] A. Bostwick, T. Ohta, T. Seyller, K. Horn, and E. Rotenberg, *Nat. Phys.* **3**, 36 (2007).
- [48] M. Sprinkle, D. Siegel, Y. Hu, J. Hicks, A. Tejada, A. Taleb-Ibrahimi, P. Le Fèvre, F. Bertran, S. Vizzini, H. Enriquez, S. Chiang, P. Soukiassian, C. Berger, W. A. de Heer, A. Lanzara, and E. H. Conrad, *Phys. Rev. Lett.* **103**, 226803 (2009).
- [49] G. Moos, C. Gahl, R. Fasel, M. Wolf, and T. Hertel, *Phys. Rev. Lett.* **87**, 267402 (2001).
- [50] Z. H. Ni, T. Yu, Z. Q. Luo, Y. Y. Wang, L. Liu, C. P. Wong, J. Miao, W. Huang, and Z. X. Shen, *ACS Nano* **3**, 569 (2009).
- [51] E. Whiteway, W. Yang, V. Yu, and M. Hilke, *Carbon* **111**, 173 (2017).
- [52] B. R. Carvalho, Y. Hao, A. Righi, J. F. Rodriguez-Nieva, L. Colombo, R. S. Ruoff, M. A. Pimenta, and C. Fantini, *Phys. Rev. B* **92**, 125406 (2015).